Chemical Engineering Journal, Volume 390, 15 June 2020, Article number 124163
DOI: 10.1016/j.cej.2020.124163

Porous MgO-stabilized CaO-based powders/pellets via a citric acid-based carbon template for thermochemical energy storage in concentrated solar power plants

Ke Wang[1,2], Feng Gu[1], Peter T. Clough[2], Pengfei Zhao[1], Edward J. Anthony[2*]

[1] School of Electrical and Power Engineering, China University of Mining and Technology, Xuzhou 221116, China.

[2] Energy and Power Theme, Cranfield University, Cranfield, Bedfordshire, MK43 0AL, UK.

Ke Wang is currently visiting Cranfield University.

* Corresponding author: Edward J. Anthony, E: b.j.anthony@cranfield.ac.uk, T: +44 (0) 1234 752 823

Abstract: The reversible $CaO/CaCO_3$ carbonation reaction (CaL) is one of the most promising candidates for high-temperature thermochemical energy storage (TCES) in concentrated solar power plants (CSP). Here, a sacrificial citric acid-based carbon template was developed to produce high-performance CaO-based sorbents to mitigate the progressive deactivation with sequential carbonation-calcination cycling. The carbon template was formed through *in situ* pyrolysis of citric acid in a simple heating process under nitrogen. After a secondary calcination step in air, a stable porous MgO-stabilized nano-CaO powder was generated and achieved high long-term effective conversion due to its resistance to pore plugging and sintering. By dry mixing citric acid with limestone-dolomite mixtures, this procedure can also be applied to synthesize MgO-stabilized CaO pellets via an extrusion–spheronization route, which resulted in comparably stable and effective conversion as the optimized CaO powder. Additionally,

the considerable mechanical strength of MgO-stabilized CaO pellets should enable their realistic application in fluidized bed reactors. Thus, this simple, cost-effective and easily-scalable synthesis technique appears to have great potential for CSP-TCES under high temperature operation.

Keywords: CO_2 capture, thermochemical energy storage, concentrated solar power

1. Introduction

The impact of rising anthropogenic CO_2 emissions, mainly derived from fossil fuel combustion, which are causing climate change, is undeniable. At the 21st Conference of Parties (COP 21), 195 participating countries committed to restrict global-mean temperature rise to well below 2 °C by 2100 [1]. To achieve such a challenging target, renewable energy technologies [2], particularly solar energy [3], must be installed on a massive scale to steadily replace fossil fuels. Due to its intrinsic intermittency, directly incorporating solar energy-derived power into an electricity grid makes the existing energy network unstable and insecure [4]. Concentrated Solar Power (CSP) [5] offers a feasible integration opportunity for large-scale thermal energy storage (TES) to produce electricity on demand, thus eliminating the intermittency problem of solar energy [6, 7]. However, current commercial CSP-TES systems based on molten salts suffer from limited thermal stability, high freezing temperature, corrosion issues, and high cost when compared with conventional fossil fuel power plants [8, 9].

A potential alternative to TES involves developing thermochemical energy storage (TCES) which operates at high temperatures, where sensible heat from solar irradiation can directly drive a reversible endothermic chemical reaction [10]. The resulting

products from this reaction are stored separately to produce power when required [11]. TCES has an inherently larger energy density, higher working temperature, and the possibility of storing energy indefinitely with negligible thermal losses compared to TES [12]. A diverse set of materials, such as metal oxides [11], sulfates [13, 14], hydroxides [15-17], and carbonates [18, 19], have been proposed for TCES. Among them, one of the most promising candidates is calcium carbonate based on the calcium looping (CaL) process [20], because of its advantages including a high working temperature (~850 °C), high energy density (~3.2 GJ/m^3), and high thermal conductivity [21]. This allows the employment of highly efficient power cycles to obtain electric efficiencies of 40–50%, plus the use of a well-documented process that is already applied in the cement and lime industry. An added, important advantage is that cheap non-toxic natural Ca-based minerals (limestone) (~$10/ton), are widely available [21]. This process relies on the cyclic carbonation/calcination reaction of $CaCO_3$ [22] as follows:

$$CaO_{(s)} + CO_{2(g)} \rightleftarrows CaCO_{3(s)} \qquad \Delta H_r = -178 \text{ kJ mol}^{-1} \quad (1)$$

The schematic diagram of CSP-CaL process recently proposed in Fig. 1. It consists of a solar calciner, a carbonation reactor, a CO_2 compression-storage system, two reservoirs for CaO and $CaCO_3$ storage, two heat exchangers, and a power unit. After calcination of $CaCO_3$ in the calciner using concentrated solar energy, the sensible heat of CaO and CO_2 is recovered through two heat exchangers and these products are stored independently. On demand, CaO and CO_2 are circulated into the carbonator wherein heat is released by the exothermic carbonation reaction. This heat is transported by the

CO_2, in excess, through different powder cycles to a gas turbine where electricity is generated while the effluent CO_2 is sent to storage. Significantly different from CaL as a CO_2 capture process (carbonation at ~650 °C under low CO_2 partial pressure of ~15 vol.% and calcination at high temperature of ~950 °C under high CO_2 concentration of ~85 vol.%), the CaL conditions in the CaL-CSP process involve carbonation at significantly high temperature (~850 °C) under pure CO_2 concentration to maximize the thermoelectric efficiency while calcination at 700-750°C performs under low CO_2 partial pressures to use of conventional volumetric receivers composed of low cost alloys [20].

However, progressive decay in CaO conversion occurs with sequential carbonation-calcination cycling, approaching low residual values (typically X~0.07) for limestone-derived CaO after 20 cycles [23]. Such CaO deactivation is a significant disadvantage for a potential CaL system integrated in a CSP plant (CSP-CaL). According to Ortiz et al. [20], large-scale equipment is, thus, needed due to the reduced CaO conversion because of the presence of high amounts of effectively inert solids in the system. Moreover, these non-reacting solids must be conveyed, preheated and cooled through the CSP plant, leading to greatly increased loss of efficiency. It was reported that the energy density of the system would be decreased from 0.89 to 0.26 GJ/m^3 as CaO residual conversion takes values from X=0.07 to X=0.05 [24]. Accompanying this effect, the overall thermal-to-electric efficiency would be lowered by 10% [25]. Thus, enhancing the CaO multicycle conversion is highly desirable and remains the main challenge in a CSP-CaL process.

It is well known that CaO deactivation is caused by significant sintering-induced loss of meso-porosity or pore plugging [26, 27]. This arises because the low Tammann temperature (T_T) of $CaCO_3$ (~529 °C) is below the typical operating temperature (~850 °C) [28]. Pore plugging is related to the rapid formation of a ~100 nm product layer of $CaCO_3$ on the surface of the CaO particles that limits further CO_2 diffusion into the unreacted core of the particles [29]. To address this issue, one effective strategy is to design porous CaO particles with a stable pore structure (high-T_T stabilizer) [30, 31]. In particular, porous MgO-stabilized CaO is promising, since MgO does not consume active CaO, unlike materials such as SiO_2 [32], Al_2O_3 [33, 34] and ZrO_2 [35], which unfortunately produce $Ca_xSi_xO_z$, $Ca_xAl_yO_z$ and $CaZrO_3$, respectively, thus reducing the available CaO. Furthermore, MgO is a cheap and environmentally benign material (e.g., in the form of dolomite). Apart from dolomite, calcium-based industrial wastes (e.g., steel slag) [36] can be another cheap and abundant source. It should be noted that preparation MgO-stabilized CaOs using organic acids have been reported widely in CaL as a CO_2 capture [37]. These MgO-stabilized CaOs applied in a CSP-CaL process were rarely examined. Recently, Sánchez Jiménez et al. [38] prepared porous $CaCO_3$-MgO composites using acetic acid-treated limestone/dolomite mixtures for high-temperature TCES. The optimized sorbent achieved a high and stable conversion (0.7 mol/mol) after 20 cycles. Unfortunately, due to its weakly acidic character, a large amount of acetic acid (8.6 mol per CaO) must be used to ensure the production of calcium/magnesium acetate precursors, making the procedure rather expensive. Moreover, these relatively large-particle-sized powders should be further examined through mechanical strength

tests to verify their suitable utilization in fluidized bed reactors.

Here, we used citric acid as a new sacrificial template to prepare porous MgO-stabilized CaO-based sorbents for high-temperature TCES. Citric acid is abundantly produced from the beverage and food industries, thus having a relatively comparable price to acetic acid. However, unlike acetic acid treatment, a smaller amount of citric acid (0.78 mol per CaO) is needed to produce soluble calcium/magnesium precursors due to its stronger acidity, which can greatly reduce the cost of synthesis. Supposing that all the carbon components in two types of organic acids was transformed into CO_2 gas, the amount of CO_2 emissions for acetic and citric acid would be 17.2 and 4.7 mol per mol of CaO, respectively. Furthermore, a carbon template can be formed through wet and/or dry mixing of citric acid with calcium/magnesium precursors followed by pyrolysis under nitrogen. Our previous studies proved that the presence of such a carbon template not only suppressed grain growth but also moderated the segregation of Ca and Mg during the high-temperature procedure [39]. This favorable morphology leads to an improved CaO conversion in TCES. More importantly, the citric acid-based carbon template was also extended to synthesize porous MgO-stabilized CaO pellets via an extrusion–spheronization route, which avoids the further addition of a carbon source during common synthesis. This route for synthesizing pellets is dry and need only employ natural limestone-dolomite mixtures, making it easily scalable. These pellets were also examined for their mechanical strength to demonstrate their suitability for use in fluidized bed reactors. To further understand the performance of such materials, a detailed structural analysis and examination of their cyclic sorption

characteristics were made to explore the underlying deactivation mechanism.

2. Experimental

2.1 Sorbents

Analytical grade $Ca(NO_3)_2{\cdot}4H_2O$ and $Mg(NO_3)_2{\cdot}6H_2O$ were used as the calcium/magnesium-based precursors to prepare MgO-stabilized CaO as fine powders. Then citric acid monohydrate was dissolved in distilled water. Calculated amounts of calcium/magnesium nitrates with various molar ratios of Ca^{2+} to Mg^{2+} were mixed with the appropriate quantities of the acid solution to obtain 100 mL total volume. The resulting solutions were then vigorously stirred into a slurry at 80 °C, and then oven-dried at 70 °C for 12 h. After drying, this acidified precursor was decomposed into a MgO-stabilized CaO powder using a two-step calcination process in a horizontal tube furnace; initially, solids were heated at 600 °C for 2 h in a N_2 atmosphere and then the temperature was raised to 800 °C for 3 h in an air atmosphere. A similar procedure using a one-step calcination process in air without the pyrolysis process in a N_2 atmosphere was also performed for comparison purposes.

Naturally-occurring limestone ($CaCO_3$ with ~1 wt% impurities) and dolomite (CaO 37.01 %, MgO 22.50 %, SiO_2 0.11 %, Fe_2O_3 0.10 %, and CO_2 balance) were first calcined in a furnace at 800 °C for 2 h under air to produce calcium and magnesium oxides for synthesizing porous MgO-stabilized CaO pellets. Subsequently, appropriate quantities of citric acid monohydrate were dry-mixed with calcium and magnesium oxides in an agate mortar, followed by pyrolysis at 600 °C for 2 h in a N_2 atmosphere. A certain amount of deionized water was added into the resulting composites to prepare

carbon-containing pellets through the extrusion–spheronization route using a E25 extruder coupled with Mini S spheronizer (Xinyite Technology Co., Ltd., China). Finally, the pellets were calcined in a furnace at 800 °C for 2 h under air to burn off the carbon template. The acquired pellets were ~1 mm. A similar procedure using natural limestone-dolomite mixture without calcination (800 °C for 2 h under air) or pyrolysis (600 °C for 2 h in a N_2 atmosphere) using the extrusion–spheronization route were prepared for comparison purposes.

The resulting sorbents were labelled as follows: the first part of the name (Ca or L) represents calcium nitrate or limestone. The second part of the name refers to the citric acid (CA) carbon template and the third part (Mg or D) represents magnesium nitrate stabilizer or dolomite. Here, the numbers refer to the molar ratio of Ca^{2+}: CA: Mg^{2+}. The "-a" means using a one-step calcination in air without pyrolysis in a N2 atmosphere, while the fourth part (B1, B2 or B3) represents synthesized pellets using a carbon template combined with the extrusion–spheronization route: B1 means the limestone-dolomite mixture was calcined in air to produce a CaO/MgO mixture that was treated with citric acid and then pyrolysed, granulated and finally calcined in air to burn off the carbon; B2 means that citric acid was added to the uncalcined limestone-dolomite mixture and then pyrolysed, granulated and finally calcined in air to burn carbon; B3 was identical to B2 but the calcination occurred after the calcination in air step. (For example, see Tables 1 and 2).

2.2 Characterization

The crystal phases of the samples were analyzed with a Bruker Model D8 Advance X-ray diffractometer (XRD) in the 2θ range of 10-90°. A Hitachi Model S-4800 scanning electron microscope (SEM) was used to record the prepared sample morphologies. The specific surface area, pore volume and size distribution were measured using a Quantachrome Novawin N_2 adsorption/desorption analyzer. Thermogravimetric analysis (TGA) and differential thermogravimetric (DTG) data for the uncalcined samples (the molar ratios of Ca to Mg were fixed at 9:1) were obtained from a Netzsch STA449C using a heating rate of 10 °C/min from ambient to 1000 °C under nitrogen. The crushing load distribution of pellets was tested by a mini-type precision compression tester (LYYS-1000N). The attrition resistance of pellets was also determined using a friability tester (CS-2) composed of a pair of symmetrical drums at a rotation speed of 25 rpm within 3000 rotations. The attrition resistance is defined as the ratio of weight loss to the initial weight of pellets. An electronic balance (±0.1 mg) was used to measure the weight loss of pellets.

2.3 Thermal energy release performance

The cyclic heat release performance of the sorbents was tested using a twin fixed-bed reactor, comprised of a carbonation reactor (100 vol.% CO_2) and a calcination reactor (100 vol.% N_2). The reacting gas was easily switched, and its flow was regulated using a mass flowmeter. A sample boat could be moved between these two reactors. Typically, the sorbent was carbonated at 850 °C for 10 min and calcined at 750 °C for 10 min.

During 20 cycles, the variation in sample weight was recorded using a delicate electronic balance (±0.1 mg). Finally, the evolution of heat release capacities as functions of time for the 1st and 20th cycles was tested in a TGA reactor (ZRY-1P, Techcomp Jingke Scientific Instrument Co., Ltd., Shanghai, China). The operating conditions were the same as those in the fixed-bed reactor. The heating and cooling rates were 10 °C/min and 15 °C/min, respectively. Finally, the thermal energy released/storage capacity (Q_r/O_s) was used to assess the cyclic activity of the prepared sorbents according the following equations:

$$Q_r\ (kJ/g_{sorbent}) = (m_1-m_2)*\Delta H_r*1000/M*m_0 \quad (2)$$

$$Q_s\ (kJ/g_{sorbent}) = (m_3-m_4)*\Delta H_r*1000/M*m_0 \quad (3)$$

where m_1 and m_2 are the instantaneous mass during carbonation, m_3 and m_4 are the instantaneous mass during calcination, ΔH_r is the enthalpy of reaction, M is the molecular weight of CO_2, and m_0 is the initial mass of CaO powder/pellets.

3. Results and discussion

3.1 Pure CaO powders

The cyclic heat release characteristics of two pure CaO samples using one-step and two-step calcination are compared in Fig. 2a. The initial heat release capacity of Ca9CA7-a was low, ~1.75 kJ/g sorbent, and it subsequently declined to ~1.0 kJ/g after 20 cycles. Upon two-step calcination, Ca9CA7 achieved a higher initial release capacity of Q_r (2.78 kJ/g), corresponding to CaO conversion of 88% and had a relatively slower deactivation rate when compared with Ca9CA7-a. The evolution of heat release/storage properties vs. time for the 1st and 20th cycles in the TGA reactor are shown in Fig. 2b.

For the heat release process, an initial fast reaction-controlled phase occurred on the surface of CaO, followed by a relatively slow diffusion-controlled phase characterized by the diffusion of CO_2 through the $CaCO_3$ product layer covering the CaO core. For the $1^{st}/20^{th}$ cycles, Ca9CA7 presented improved Q_r capacity in both reaction-controlled and diffusion-controlled phases as compared with Ca9CA7-a. The improved characteristics were also observed in the heat storage curves. Based on these results, we believe that an additional pyrolysis process in the preparation route may generate the improved cyclic release heat characteristics of Ca9CA7, in agreement with the results of CaO sorbents derived from the organometallic calcium-based carbon template route [40].

To confirm this hypothesis, the following TGA, SEM, XRD and BET characterizations were performed. First, the thermogram (Fig. 3) of uncalcined citric acid-modified sample with the molar ratio of Ca^{2+} to citric acid of 9:7 was examined by heating the samples from ambient to 1000 °C at 10 °C/min under nitrogen. Both TGA and DTG curves showed the presence of a three-step decomposition process. In the first step (around 5% mass loss), dehydration of the sorbent finished at around 100 °C. The second mass loss (approximately 65% of the total mass) took place from 104 °C to 570 °C, due to the decomposition of citric acid mixtures into intermediate compounds ($CaCO_3$, CO_2, H_2O, anhydride and ketone). There were two obvious weight losses, which could be related to the formation of both anhydride and ketone [41, 42]. Finally, the last mass loss (about 12%) was complete by ~710 °C, and can be attributed to the decomposition of $CaCO_3$ to yield CaO. It was also worth noting that the deposited

carbon was due to the pyrolysis under nitrogen. Based on the initial organic content and the final weight, the final carbon content of this sample is ~26.5 wt%.

The SEM image of the resulting carbon-containing composites (Fig. 4a) shows a thin sheet-like structure with nonporous surface. This architecture acts as a sacrificial template for producing a well-developed macroporous sheet-like morphology with separated nano-sized particles (~90 nm) in Ca9CA7 (Fig. 4b). However, this sheet-like architecture was absent in Ca9CA7-a with relatively large and compact aggregates, indicating that this carbon template also served as a physical dispersant to effectively suppress particle aggregation. The XRD patterns were further examined and as shown in Fig. 5, the two materials had the same characteristic peaks of highly crystalline CaO. The average crystallite size of CaO was estimated using the Scherrer's equation: $D\ (nm) = k\lambda/\beta \cos\theta$, where k is the Scherrer constant (k=0.89), λ is the wavelength of X-rays (λ=0.015 nm), β is the full width at half maximum, and θ is the diffraction angle. The crystal size of Ca9CA7-a (123.8 nm) was relatively larger than that of Ca9CA7 (113.6 nm), suggesting that the presence of the carbon template helped to reduce the CaO crystal size. The N_2 adsorption results of two CaO samples are also shown in Table 1. The specific surface area and pore volume of Ca9CA7 were both higher than those of Ca9CA7-a. The N_2 adsorption results agreed well with SEM and XRD characterizations, suggesting that with the help of the carbon template, Ca9CA7 had smaller CaO crystallite/particle sizes, a more porous structure, and larger specific surface area, leading to its higher performance. On the other hand, the uncalcined citric acid-modified sample showed a thin sheet morphology composed of smaller nano-$CaCO_3$

grains embedded into the carbon network. During the calcination step, to away the burn carbon, the structure of the sorbent tended to undergo partial reorganization or slight growth and agglomeration of crystal grains, which is consistent with the reported literature using other carbon templates [43, 44]. However, Ca9CA7 still preserved the sheet morphology while the architectural structure of Ca9CA7-a collapsed.

The heat release properties of pure CaO modified by three ratios of citric acid during 20 cycles is shown in Fig. 6a. When the amount of citric acid was low, Ca9CA5 had the lowest initial Q_r (2.40 kJ/g) and demonstrated a more noticeable decay compared to the other sorbents. When the amount of citric acid was further increased to 9:7 (Ca9CA7), the sorbent achieved not only the highest value of Q_r (2.78 kJ/g) but also the slowest decay rate among the four samples. However, when the amount of citric acid was increased to 9:9, the heat release properties of Ca9CA9 deteriorated with a relatively low initial Q_r and evidently faster decay. Their evolution of heat release/storage curves vs. time for the 1^{st} and 20^{th} cycles in the TGA reactor are shown in Fig. 6b. For the $1^{st}/20^{th}$ cycles, Ca9CA7 presented the highest values of Q_r/O_s among the four samples, consistent with the results from the fixed-bed reactor. Thus, the optimal amount of citric acid determined here was a 9:7 ratio.

To explore underlying deactivation mechanisms responsible for the behavior of these four samples, a series of characterization tests were conducted. Fig. 5 shows the XRD patterns of three sorbents modified with different ratios of citric acid. The crystal size of Ca9CA5 (121 nm) was relatively larger than that of Ca9CA7 (94 nm), suggesting that the presence of more deposited carbon could effectively suppress crystal

growth of CaO. However, too much deposited carbon induced increased crystal growth of CaO since the crystal size of Ca9CA9 (114 nm) was greater than that of Ca9CA7. The SEM images of pure CaO using different ratios of citric acid are presented in Fig. 7. Ca9CA5 (Fig. 7a) appeared as sintered agglomerates due to the low ratio of citric acid. However, with a high content of citric acid, Ca9CA7 (Fig. 7b) presented a macroporous sheet-like morphology composed of ~90 nm sized particles. However, as the amount further increased to 9:9, Ca9CA9 (Fig. 7c) showed the largest sized sintered agglomerates among the three samples, indicating that the addition of excessive citric acid is detrimental to generating a porous morphology. According to Liu's work [45], at excessive concentrations of carbohydrates (i.e. citric acid), a carbon network with thick walls was formed rather than a sheet-like carbon formed at low carbon concentrations during the pyrolysis process. This morphology may induce the agglomeration growth of $CaCO_3$, further seeding the crystal growth of CaO. On the other hand, at high concentrations of citric acid, a large amount of heat had to be released during preparation process, which evidently led to the crystal growth of CaO. The N_2 adsorption results of these three samples are shown in Table 1. The specific surface area and pore volume of Ca9CA7 were highest among the three samples. In particular, the specific surface area of Ca9CA7 was ~1.5 times as large as that of Ca9CA5. The N_2 adsorption results agreed well with SEM and XRD characterizations, suggesting that the suitable amount of citric acid was added to generate the smallest CaO crystallite/particle sizes and the greatest porous structure, and largest specific surface area, contributing to the highest performance of Ca9CA7. Unfortunately, this

porous structure was not maintained after 20 cycles and, instead, sintered agglomerates were evident, implying its relatively reduced performance of cycled Ca9CA7 in Fig. 7d and the absence of a structure stabilizer.

3.2 MgO-stabilized CaO powders

To improve the cyclic heat release capacity of Ca9CA7, MgO was used as an inert stabilizer through the carbon template method. Fig. 8a compares cyclic heat release capacity of two MgO-stabilized CaO samples with that of Ca9CA7. MgO-containing sorbents exhibited a stable heat release capacity, whereas the pure CaO (Ca9CA7) sample showed a characteristic decay with 20 repeated cycles, confirming the important role of the MgO. Moreover, when the molar ratios of Ca to Mg decrease from 9:1 to 8:2, the two MgO-stabilized samples presented a similar stable cyclic behavior, suggesting that increasing the MgO content beyond 10 mol% does not enhance the cyclic stability further. Thus, the optimized MgO content appears to be no more than 10 mol%. As further shown in the evolution of heat release/storage curves vs. time (Fig. 8b), Ca9CA7Mg1 exhibited almost the same values of Q_r/O_s as the pure CaO sample (Ca9CA7) despite the presence of inert MgO on the first cycle. The values of Q_r/O_s for Ca9CA7Mg1 were even higher than Ca9CA7 on the 20^{th} cycle, which indicated its higher and more stable release/storage heat performance.

A series of characterizations were conducted to explain the cyclic sorption characteristics of Ca9CA7Mg1. The main crystalline phases of uncalcined MgO-stabilized sample were $CaCO_3$ (Fig. 9), although an amorphous C (002) peak around 17 degrees was also evident, suggesting that the carbon template was generated during

pyrolysis, as it was not present in the calcined sample. Interestingly, the phase of MgO was not detected by XRD. Thus, we speculated that MgO may be present as an amorphous phase and similar results were also observed by our previous study [39]. Moreover, compared with the case of unsupported CaO, the presence of MgO also dramatically affected the crystallite size of CaO (49 nm). Furthermore, both specific surface area and pore volume of Ca9CA7Mg1 were larger than those of Ca9CA7 (Table 1), proving that the presence of MgO improved the porous structure of pure CaO. Ca9CA7Mg1 presented relatively regular and smaller nano-sized CaO particles (Fig. 10a). Moreover, Ca9CA7Mg1 also exhibited a more macroporous structure, in agreement with BET results. Additionally, the SEM image of cycled Ca9CA7Mg1 (Fig. 10b) also retained its highly macroporous structure. Based on these characterization results, the highly stable performance of Ca9CA7Mg1 seems to be due to its resistance to pore-plugging and sintering as a result of the presence of smaller CaO crystallite/particle sizes, more porous structure, larger specific surface area, and the presence of the MgO stabilizer.

3.3 *MgO-stabilized CaO powders and pellets*

The synthesis conditions (two-step calcination, acid content and MgO content) greatly affect the cyclic heat release properties and have important implications for practical applications, and these were examined. First, instead of calcium/magnesium nitrates dissolved in citric acid solution, dry-mixing of citric acid with natural Ca-based minerals (limestone-dolomite mixtures) and a further two-step calcination were extended for preparation of MgO-stabilized CaO powders. The cyclic heat release

properties of MgO-stabilized CaO powders using three ratios of citric acid addition, over 20 cycles are shown in Fig. 11a. All of these three powders presented relatively stable performance due to the presence of the MgO stabilizer derived from dolomite. However, their initial Q_r values varied with the amount of citric acid. When the amount of citric acid was low, L8CA5D1 had the lowest initial Q_r (2.12 kJ/g) among the three powders. When the amount was increased to 9:7, L8CA7D1 exhibited the highest values of Q_r (2.78 kJ/g). However, when the amount was further increased to 9:9, the initial Q_r of L8CA9D1 was lower than that of L8CA7D1. Thus, the optimal amount of citric acid (9:7) should be added when using limestone-dolomite mixtures as CaO precursor, which is the same as that when using calcium/magnesium nitrates. It seems that the two routes may follow the same synthesis principle. It also should be noted that the values of initial Q_r for limestone-dolomite mixtures are slightly lower than that for calcium/magnesium nitrates, which was mainly caused by the sintering of impurities (such as alkali metals) in limestone-dolomite mixtures. As shown in Fig. 12a, the SEM image of fresh L8CA7D1 presented a macroporous structure. The presence of slightly sintered agglomerates was also observed. A similar morphology was reported by previous studies using natural limestone containing a small amount of a Na ion [46].

Calcium nitrate, magnesium nitrate and citric acid are uniformly mixed on an ion scale in the wet mixing method. While in dry mixing method, limestone-dolomite mixture was firstly calcined in air to produce CaO-MgO to enhance the alkalinity. Then CaO-MgO mixed with citric acid undergoes the pyrolysis process, during which, an acid-alkali reaction between CaO-MgO and citric acid occurred to first form a citrate

salt, where Ca and Mg uniformly mixed on an ion scale. With the help of uniform mixing, L8CA7D1 presented a comparably stable and effective conversion as Ca9CA7Mg1. Thus, wet mixing was more uniform, while dry mixing was more suitable for industrial applications.

Subsequently, this dry mixing procedure coupled with an extrusion–spheronization route was used to synthesize MgO-stabilized CaO pellets. The cyclic heat release properties of MgO-stabilized CaO pellets using different pelletization processes during 20 cycles is shown in Fig. 11b. The cyclic performance for L8CA7D1 is also presented for comparison. Without transformation from limestone-dolomite mixtures to CaO-MgO mixtures upon the initial calcination process, L8CA7D1-B3 demonstrated the most unstable performance as its initial Q_r of 2.32 kJ/g decreased to 1.64 kJ/g after 20 cycles. This poor cyclic performance was most likely due to an incomplete reaction between limestone-dolomite mixtures and citric acid during pyrolysis, considering the weaker alkalinity of $CaCO_3$/$CaCO_3$.$MgCO_3$ mixtures in comparison with CaO-MgO mixtures. Without pyrolysis during the pelletization, L8CA7D1-B2 exhibited a low value (2.28 kJ/g) for initial Q_r, mainly due to the reduced porosity from the intense extrusion in the extrusion–spheronization route. As confirmed by the SEM image shown in Fig. 12b, the amount of macropores on the surface of fresh L8CA7D1-B2 decreased dramatically. To overcome the side effect of extrusion–spheronization, an additional carbon source as pore-expanding agent was used in previous studies making their pelletization process more costly and complex [47, 48]. A simple and cheaper strategy is using the carbon template formed through *in situ*

pyrolysis. As demonstrated in Fig. 11b-c, L8CA7D1-B1 achieved higher and more stable heat release performance as compared with L8CA7D1-B2 and L8CA7D1-B3. Moreover, such high performance was even comparable to that of L8CA7D1. The evolution of heat release/storage curves vs. time further confirmed that L8CA7D1-B1 achieved nearly identical values of Q_r/O_s to L8CA7D1 for the $1^{st}/20^{th}$ cycles.

XRD (Fig. 9), BET (Table 1) and SEM (Fig. 12) characterizations were further employed to validate the cyclic release heat characteristics of L8CA7D1-B1. XRD showed that the main crystalline phase was CaO, whereas no MgO was detected. Furthermore, both specific surface area and pore volume for L8CA7D1-B1 were lower than those of Ca9CA7Mg1, probably caused by the presence of impurities in limestone-dolomite mixtures. However, this value was larger than that for MgO-stabilized CaO pellets reported in previous studies [47, 48], suggesting that the porous structure was preserved by the presence of the carbon template during extrusion–spheronization. Moreover, L8CA7D1-B1 (Fig. 12c) also exhibited a macroporous structure, agreeing well with BET results. Additionally, the SEM image of cycled L8CA7D1-B1 (Fig. 12d) also retained its highly macroporous structure.

Besides cyclic release heat properties, mechanical strength is also an essential parameter for pellets to assess their application in fluidized bed reactors. When pellets with low mechanical strength are introduced into a fluidized bed reactor, they tend to be broken into smaller fragments and are likely to be elutriated during repeated energy storage/release cycles, which represents inefficient usage of pellets. Hence, we have determined the mechanical strength including crushing load distribution and attrition

resistance of three as-prepared pellets.

The crushing load distribution for the three pellets is shown in Fig. 13. The crushing loads of these pellets are all approximately normally distributed. The average crushing load of L8CA7D1-B3 (Fig. 13a) was the lowest (2.7 N) among the pellets due to lack of a complete pyrolysis reaction between limestone-dolomite mixtures and citric acid. L8CA7D1-B2 (Fig. 13b) showed a much higher average crushing load of 10.1 N, owing to the improved extrusion force caused by a complete pyrolysis reaction. This value is comparable to that for the reported CaO-based pellets [49]. Interestingly, L8CA7D1-B1 (Fig. 13c) presented an even higher average crushing load (47.3 N) than that of L8CA7D1-B2, and this is the highest value reported in the open literature [49, 50] and is 40 times as large as the minimum suitable value for a realistic fluid bed reactors (> 1 N). The comparisons of the calculated compression strength per unit area of these pellets are further summarized in Fig. 13(d). The compression strength can be ranked as follows: L8CA7D1-B1 (60.3 MPa)≫ L8CA7D1-B2 (12.9 MPa)> L8CA7D1-B1 (3.4 MPa). The CaO-based powders used in the common extrusion–spheronization route primarily consisted of CaO, which is similar to our L8CA7D1-B2. A moderate amount of deionized water was needed to form a paste for further efficient extrusion. This hydration reaction was widely reported to reduce the mechanical strength [51]. However, the CaO-based powders used in the case of L8CA7D1-B1 were carbon-containing $CaCO_3$ (Fig. 5) and, thus, eliminated this unfavorable effect, giving L8CA7D1-B1 the highest average crushing load.

The attrition resistance of these three pellets was also determined and the results

are shown in Table 2. It is clear that the attrition resistance can be ranked as L8CA7D1-B1≫L8CA7D1-B2≫L8CA7D1-B3, agreeing with the results of the crushing load distribution test. After 1000 cycles, L8CA7D1-B3 presented the highest weight loss (6.36%) whereas the value for L8CA7D1-B1 was only 1.08%, which is ~1/6 that of L8CA7D1-B3. After 3000 cycles, the weight loss of L8CA7D1-B3 was 11.49% and seemed to be increasing in further cycles. By comparison, the weight loss of L8CA7D1-B1 finally reached only 2.12% after 3000 cycles.

4. Conclusions

A simple cost-effective and scalable synthesis technique to yield highly efficient MgO-stabilized CaO sorbents was developed. The presence of citric acid served as a carbon template to suppress grain growth, moderate the segregation of Ca and Mg and improve porous structure, in turn mitigating pore-plugging and sintering. Thus, a high capacity and stable cyclic performance for MgO-stabilized CaO powders was obtained. Moreover, for dry-mixing of citric acid with limestone-dolomite mixtures, this carbon template integrated with extrusion–spheronization for preparing the MgO-stabilized CaO pellet is associated with negligible capacity losses over 20 repeated cycles as compared to the optimized CaO powder. Additionally, this pellet showed high crushing load distribution and low weight loss, suggesting the strong mechanical strength and, therefore, making it suitable for use in fluidized bed reactors. The high capacity, stable cyclic performance and strong mechanical strength are required for CSP-TCES in high temperature operation.

Acknowledgement

Financial support for this work from the Fundamental Research Funds for the Central Universities (2018XKQYMS13) is gratefully acknowledged.

References

[1] C.J. Rhodes, The 2015 Paris Climate Change Conference: COP21, Sci. Prog. 99 (2016) 97-104.
[2] J. Lian, Y. Zhang, C. Ma, Y. Yang, E. Chaima, A review on recent sizing methodologies of hybrid renewable energy systems, Energy Convers. Manage. 199 (2019) 112027.
[3] S. Badakhshan, N. Hajibandeh, M. Shafie-khah, J.P.S. Catalão, Impact of solar energy on the integrated operation of electricity-gas grids, Energy 183 (2019) 844-853.
[4] R.K. de_Richter, T. Ming, S. Caillol, W. Liu, Fighting global warming by GHG removal: Destroying CFCs and HCFCs in solar-wind power plant hybrids producing renewable energy with no-intermittency, Int. J. Greenhouse Gas Control 49 (2016) 449-472.
[5] A. Peinado Gonzalo, A. Pliego Marugán, F.P. García Márquez, A review of the application performances of concentrated solar power systems, Appl. Energy 255 (2019) 113893.
[6] M. Gonzalez, U. Nithiyanantham, E. Carbó-Argibay, O. Bondarchuk, Y. Grosu, A. Faik, Graphitization as efficient inhibitor of the carbon steel corrosion by molten binary nitrate salt for thermal energy storage at concentrated solar power, Sol. Energy Mater. Sol. Cells 203 (2019) 110172.
[7] H. Chirino, B. Xu, X. Xu, Parametric study of cascade latent heat thermal energy storage (CLHTES) system in Concentrated Solar Power (CSP) plants, Journal of the Energy Institute 92 (2019) 653-664.
[8] S. Bell, T. Steinberg, G. Will, Corrosion mechanisms in molten salt thermal energy storage for concentrating solar power, Renewable Sustainable Energy Rev. 114 (2019) 109328.
[9] C. Parrado, A. Marzo, E. Fuentealba, A.G. Fernández, 2050 LCOE improvement using new molten salts for thermal energy storage in CSP plants, Renewable Sustainable Energy Rev. 57 (2016) 505-514.
[10] J. Sunku Prasad, P. Muthukumar, F. Desai, D.N. Basu, M.M. Rahman, A critical review of high-temperature reversible thermochemical energy storage systems, Appl. Energy 254 (2019) 113733.
[11] H.B. Dizaji, H. Hosseini, A review of material screening in pure and mixed-metal oxide thermochemical energy storage (TCES) systems for concentrated solar power (CSP) applications, Renewable Sustainable Energy Rev. 98 (2018) 9-26.
[12] S. Wu, C. Zhou, E. Doroodchi, R. Nellore, B. Moghtaderi, A review on high-temperature thermochemical energy storage based on metal oxides redox cycle, Energy Convers. Manage. 168 (2018) 421-453.
[13] Q. Wang, Y. Xie, B. Ding, G. Yu, F. Ye, C. Xu, Structure and hydration state characterizations of $MgSO_4$-zeolite 13x composite materials for long-term thermochemical heat storage, Sol. Energy Mater. Sol. Cells 200 (2019) 110047.
[14] D. Mahon, G. Claudio, P.C. Eames, An experimental investigation to assess the potential of using $MgSO_4$ impregnation and Mg^{2+} ion exchange to enhance the performance of 13X molecular sieves for interseasonal domestic thermochemical energy storage, Energy Convers. Manage. 150 (2017) 870-877.
[15] Y. Yuan, Y. Li, L. Duan, H. Liu, J. Zhao, Z. Wang, $CaO/Ca(OH)_2$ thermochemical heat storage of carbide slag from calcium looping cycles for CO2 capture, Energy Convers. Manage. 174 (2018) 8-19.
[16] Y.A. Criado, A. Huille, S. Rougé, J.C. Abanades, Experimental investigation and model validation of a $CaO/Ca(OH)_2$ fluidized bed reactor for thermochemical energy storage applications, Chem. Eng. J. 313 (2017) 1194-1205.

[17] Q. Ranjha, N. Vahedi, A. Oztekin, High-temperature thermochemical energy storage – heat transfer enhancements within reaction bed, Appl. Therm. Eng. 163 (2019) 114407.
[18] L. André, S. Abanades, Investigation of metal oxides, mixed oxides, perovskites and alkaline earth carbonates/hydroxides as suitable candidate materials for high-temperature thermochemical energy storage using reversible solid-gas reactions, Materials Today Energy 10 (2018) 48-61.
[19] L. André, S. Abanades, Evaluation and performances comparison of calcium, strontium and barium carbonates during calcination/carbonation reactions for solar thermochemical energy storage, Journal of Energy Storage 13 (2017) 193-205.
[20] C. Ortiz, J.M. Valverde, R. Chacartegui, L.A. Perez-Maqueda, P. Giménez, The Calcium-Looping ($CaCO_3$/CaO) process for thermochemical energy storage in Concentrating Solar Power plants, Renewable Sustainable Energy Rev. 113 (2019) 109252.
[21] J.M. Valverde, The Ca-looping process for CO_2 capture and energy storage: role of nanoparticle technology, J. Nanopart. Res. 20 (2018) 39.
[22] G. Flamant, D. Hernandez, C. Bonet, J.-P. Traverse, Experimental aspects of the thermochemical conversion of solar energy; Decarbonation of $CaCO_3$, Sol. Energy 24 (1980) 385-395.
[23] B. Sarrion, J.M. Valverde, A. Perejon, L. Perez-Maqueda, P.E. Sanchez-Jimenez, On the Multicycle Activity of Natural Limestone/Dolomite for Thermochemical Energy Storage of Concentrated Solar Power, Energy Technology 4 (2016) 1013-1019.
[24] C. Ortiz, M.C. Romano, J.M. Valverde, M. Binotti, R. Chacartegui, Process integration of Calcium-Looping thermochemical energy storage system in concentrating solar power plants, Energy 155 (2018) 535-551.
[25] R. Chacartegui, A. Alovisio, C. Ortiz, J.M. Valverde, V. Verda, J.A. Becerra, Thermochemical energy storage of concentrated solar power by integration of the calcium looping process and a CO_2 power cycle, Appl. Energy 173 (2016) 589-605.
[26] L. Fedunik-Hofman, A. Bayon, J. Hinkley, W. Lipiński, S.W. Donne, Friedman method kinetic analysis of CaO-based sorbent for high-temperature thermochemical energy storage, Chem. Eng. Sci. 200 (2019) 236-247.
[27] H. Sun, Y. Li, Z. Bian, X. Yan, Z. Wang, W. Liu, Thermochemical energy storage performances of Ca-based natural and waste materials under high pressure during CaO/$CaCO_3$ cycles, Energy Convers. Manage. 197 (2019) 111885.
[28] B. Sarrión, A. Perejón, P.E. Sánchez-Jiménez, L.A. Pérez-Maqueda, J.M. Valverde, Role of calcium looping conditions on the performance of natural and synthetic Ca-based materials for energy storage, Journal of CO_2 Utilization 28 (2018) 374-384.
[29] M. Benitez-Guerrero, J.M. Valverde, P.E. Sanchez-Jimenez, A. Perejon, L.A. Perez-Maqueda, Multicycle activity of natural $CaCO_3$ minerals for thermochemical energy storage in Concentrated Solar Power plants, Sol. Energy 153 (2017) 188-199.
[30] R. Han, J. Gao, S. Wei, Y. Su, F. Sun, G. Zhao, Y. Qin, Strongly coupled calcium carbonate/antioxidative graphite nanosheets composites with high cycling stability for thermochemical energy storage, Appl. Energy 231 (2018) 412-422.
[31] Y. Da, Y. Xuan, L. Teng, K. Zhang, X. Liu, Y. Ding, Calcium-based composites for direct solar-thermal conversion and thermochemical energy storage, Chem. Eng. J. (2019) 122815.
[32] X. Chen, X. Jin, Z. Liu, X. Ling, Y. Wang, Experimental investigation on the CaO/CaCO3 thermochemical energy storage with SiO2 doping, Energy 155 (2018) 128-138.
[33] M. Benitez-Guerrero, J.M. Valverde, P.E. Sanchez-Jimenez, A. Perejon, L.A. Perez-Maqueda,

Calcium-Looping performance of mechanically modified Al_2O_3-CaO composites for energy storage and CO_2 capture, Chem. Eng. J. 334 (2018) 2343-2355.
[34] J. Obermeier, K.G. Sakellariou, N.I. Tsongidis, D. Baciu, G. Charalambopoulou, T. Steriotis, K. Müller, G. Karagiannakis, A.G. Konstandopoulos, A. Stubos, W. Arlt, Material development and assessment of an energy storage concept based on the CaO-looping process, Sol. Energy 150 (2017) 298-309.
[35] B. Sarrion, P.E. Sanchez-Jimenez, A. Perejon, L.A. Perez-Maqueda, J.M. Valverde, Pressure Effect on the Multicycle Activity of Natural Carbonates and a Ca/Zr Composite for Energy Storage of Concentrated Solar Power, ACS Sustainable Chemistry & Engineering 6 (2018) 7849-7858.
[36] S. Tian, J. Jiang, F. Yan, K. Li, X. Chen, V. Manovic, Highly efficient CO_2 capture with simultaneous iron and CaO recycling for the iron and steel industry, Green Chemistry 18 (2016) 4022-4031.
[37] M. Erans, V. Manovic, E.J. Anthony, Calcium looping sorbents for CO_2 capture, Appl. Energy 180 (2016) 722-742.
[38] P.E. Sánchez Jiménez, A. Perejón, M. Benítez Guerrero, J.M. Valverde, C. Ortiz, L.A. Pérez Maqueda, High-performance and low-cost macroporous calcium oxide based materials for thermochemical energy storage in concentrated solar power plants, Appl. Energy 235 (2019) 543-552.
[39] K. Wang, P.T. Clough, P. Zhao, E.J. Anthony, Synthesis of highly effective stabilized CaO sorbents via a sacrificial N-doped carbon nanosheet template, Journal of Materials Chemistry A 7 (2019) 9173-9182.
[40] P. Zhao, J. Sun, Y. Li, K. Wang, Z. Yin, Z. Zhou, Z. Su, Synthesis of Efficient CaO Sorbents for CO_2 Capture Using a Simple Organometallic Calcium-Based Carbon Template Route, Energy Fuels 30 (2016) 7543-7550.
[41] J.A. Ávila Ramírez, E. Fortunati, J.M. Kenny, L. Torre, M.L. Foresti, Simple citric acid-catalyzed surface esterification of cellulose nanocrystals, Carbohydr. Polym. 157 (2017) 1358-1364.
[42] X. Li, G. Li, J. Li, Y. Yu, Y. Feng, Q. Chen, S. Komarneni, Y. Wang, Producing petrochemicals from catalytic fast pyrolysis of corn fermentation residual by-products generated from citric acid production, Renewable Energy 89 (2016) 331-338.
[43] M. Broda, C.R. Mueller, Synthesis of Highly Efficient, Ca-Based, Al_2O_3-Stabilized, Carbon Gel-Templated CO_2 Sorbents, Adv. Mater. 24 (2012) 3059-3064.
[44] M.A. Naeem, A. Armutlulu, Q. Imtiaz, F. Donat, R. Schäublin, A. Kierzkowska, C.R. Müller, Optimization of the structural characteristics of CaO and its effective stabilization yield high-capacity CO_2 sorbents, Nature Communications 9 (2018) 2408.
[45] X. Liu, C. Giordano, M. Antonietti, A Facile Molten-Salt Route to Graphene Synthesis, Small 10 (2014) 193-200.
[46] H.R. Radfarnia, M.C. Iliuta, Limestone Acidification Using Citric Acid Coupled with Two-Step Calcination for Improving the CO_2 Sorbent Activity, Ind. Eng. Chem. Res. 52 (2013) 7002-7013.
[47] H. Li, M. Qu, Y. Yang, Y. Hu, W. Liu, One-step synthesis of spherical CaO pellets via novel graphite-casting method for cyclic CO_2 capture, Chem. Eng. J. 374 (2019) 619-625.
[48] X. Tong, W. Liu, Y. Yang, J. Sun, Y. Hu, H. Chen, Q. Li, A semi-industrial preparation procedure of CaO-based pellets with high CO_2 uptake performance, Fuel Process. Technol. 193 (2019) 149-158.
[49] J. Sun, W. Liu, Y. Hu, J. Wu, M. Li, X. Yang, W. Wang, M. Xu, Enhanced performance of extruded–spheronized carbide slag pellets for high temperature CO_2 capture, Chem. Eng. J. 285 (2016) 293-303.
[50] J. Sun, W. Liu, Y. Hu, M. Li, X. Yang, Y. Zhang, M. Xu, Structurally Improved, Core-in-Shell, CaO-Based Sorbent Pellets for CO_2 Capture, Energy Fuels 29 (2015) 6636-6644.

[51] V. Materić, S. Edwards, S.I. Smedley, R. Holt, $Ca(OH)_2$ Superheating as a Low-Attrition Steam Reactivation Method for CaO in Calcium Looping Applications, Ind. Eng. Chem. Res. 49 (2010) 12429-12434.

Table 1. N_2 adsorption/desorption results of samples

Samples	Surface area (m^2/g)	Pore volume (cc/g)	Average pore diameter (nm)
Ca9CA5	8.5	0.067	23
Ca9CA7	12.9	0.28	34
Ca9CA9	9.2	0.25	38
Ca9CA7Mg1	20.6	0.62	29
L8CA7D1-B1	8.6	0.063	29

Table 2. The attrition resistance of three pellets

Pellets	Weight loss (wt%)		
	After 1000 rotations	After 2000 rotations	After 3000 rotations
L8CA7D1-B1	1.08	1.86	2.12
L8CA7D1-B2	3.95	6.19	8.65
L8CA7D1-B3	6.36	9.35	11.49

Figure captions:

Fig. 1. The schematic diagram of CSP-CaL process.

Fig. 2. The cyclic release heat capacity during 20 cycles in the FB reactor using two types of calcination (a) and the evolution of heat release capacities in the TG reactor for 1st and 20th cycles using two types of calcination (b).

Fig. 3. The thermograms of an uncalcined citric acid-modified sample.

Fig. 4. SEM images of different samples: (a) uncalcined citric acid-modified sample, (b) Ca9CA7 and (c) Ca9CA7-a.

Fig. 5. XRD patterns of several pure CaO powders with their CaO crystallite sizes.

Fig. 6. The cyclic release heat capacity during 20 cycles in the FB reactor using three different amounts of citric acid (a) and the evolution of heat release capacities in the TG reactor for 1st and 20th cycles using different amounts of citric acid (b).

Fig. 7. SEM images of several CaO samples: (a) fresh Ca9CA5, (b) fresh Ca9CA7, (c) fresh Ca9CA9, and (d) cycled Ca9CA7.

Fig. 8. The cyclic release heat capacity during 20 cycles in the FB reactor (a) and the evolution of heat release capacities in the TG reactor for 1^{st} and 20^{th} cycles (b).

Fig. 9. XRD patterns of two sorbents.

Fig. 10. SEM images of two MgO-stabilized CaO powders: (a) fresh Ca9CA7Mg1 and (b) cycled Ca9CA7Mg1.

Fig. 11. The cyclic release heat capacity during 20 cycles in the FB reactor for several MgO-stabilized CaO powders (a) and pellets (b) and the evolution of heat release

capacities for two pellets in the TG reactor for 1st and 20th cycles (c).

Fig. 12. SEM images of several MgO-stabilized CaO powders/pellets: (a) fresh L8CA7D1, (b) L8CA7D1-B2, (c) L8CA7D1-B1 and (d) cycled L8CA7D1-B1.

Fig. 13. The crushing load distribution of three pellets: (a) L8CA7D1-B3, (b) L8CA7D1-B2, (c) L8CA7D1-B1and the comparisons of the calculated compression strength of these pellets (d).

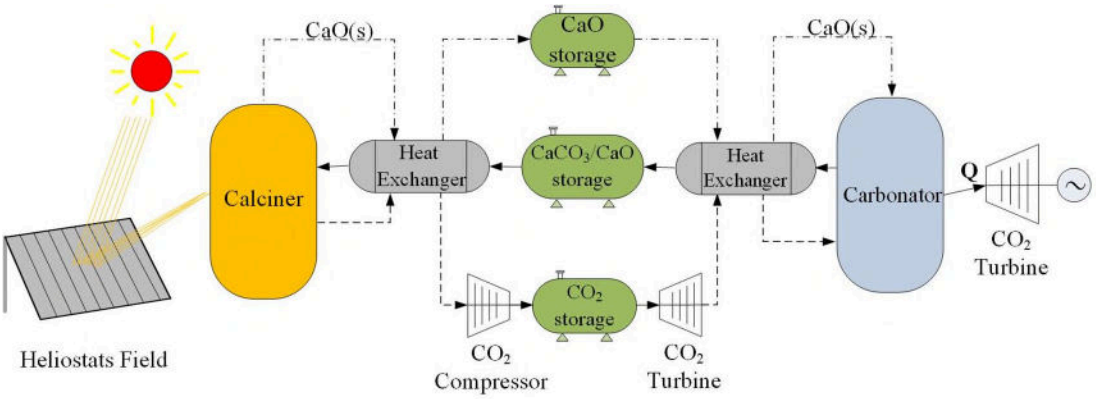
CaO(s)
CaO storage
CaO(s)
Heat Exchanger
CaCO3/CaO storage
Heat Exchanger
Calciner
Carbonator
Q
CO2 Turbine
CO2 storage
Heliostats Field
CO2 Compressor
CO2 Turbine

Fig. 1

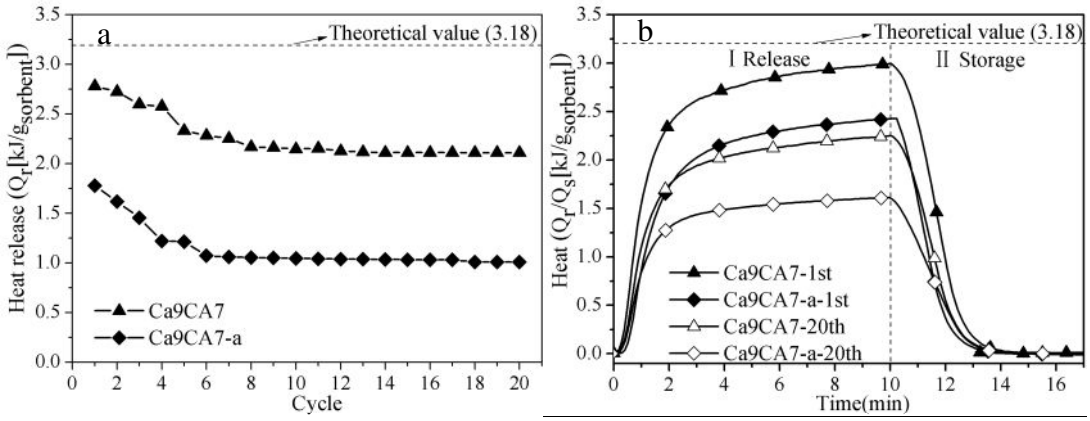
a
Theoretical value (3.18)
Heat release (Q_r[kJ/$g_{sorbent}$])
Cycle
Ca9CA7
Ca9CA7-a
b
Theoretical value (3.18)
I Release
II Storage
Heat (Q_r/Q_s[kJ/$g_{sorbent}$])
Time(min)
Ca9CA7-1st
Ca9CA7-a-1st
Ca9CA7-20th
Ca9CA7-a-20th

Fig.2

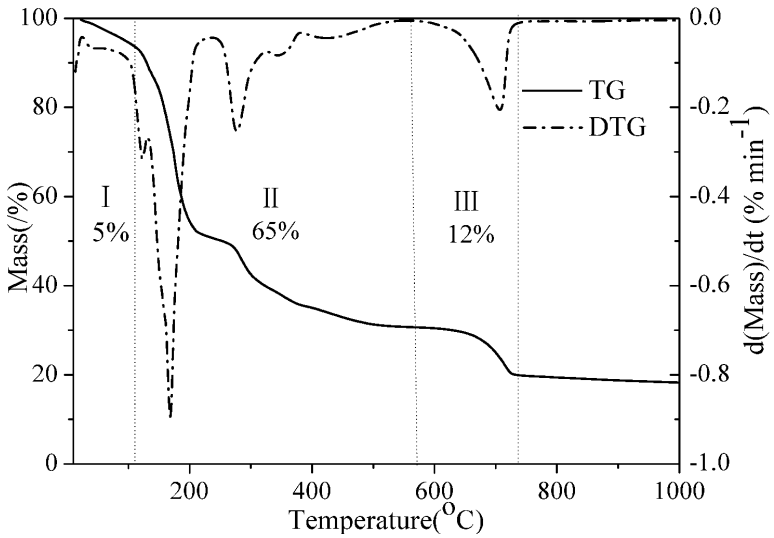
100
80
60
40
20
0
0.0
-0.2
-0.4
-0.6
-0.8
-1.0
200
400
600
800
1000
Mass(/%)
d(Mass)/dt (% min-1)
Temperature(OC)
TG
DTG
I
5%
II
65%
III
12%

Fig. 3

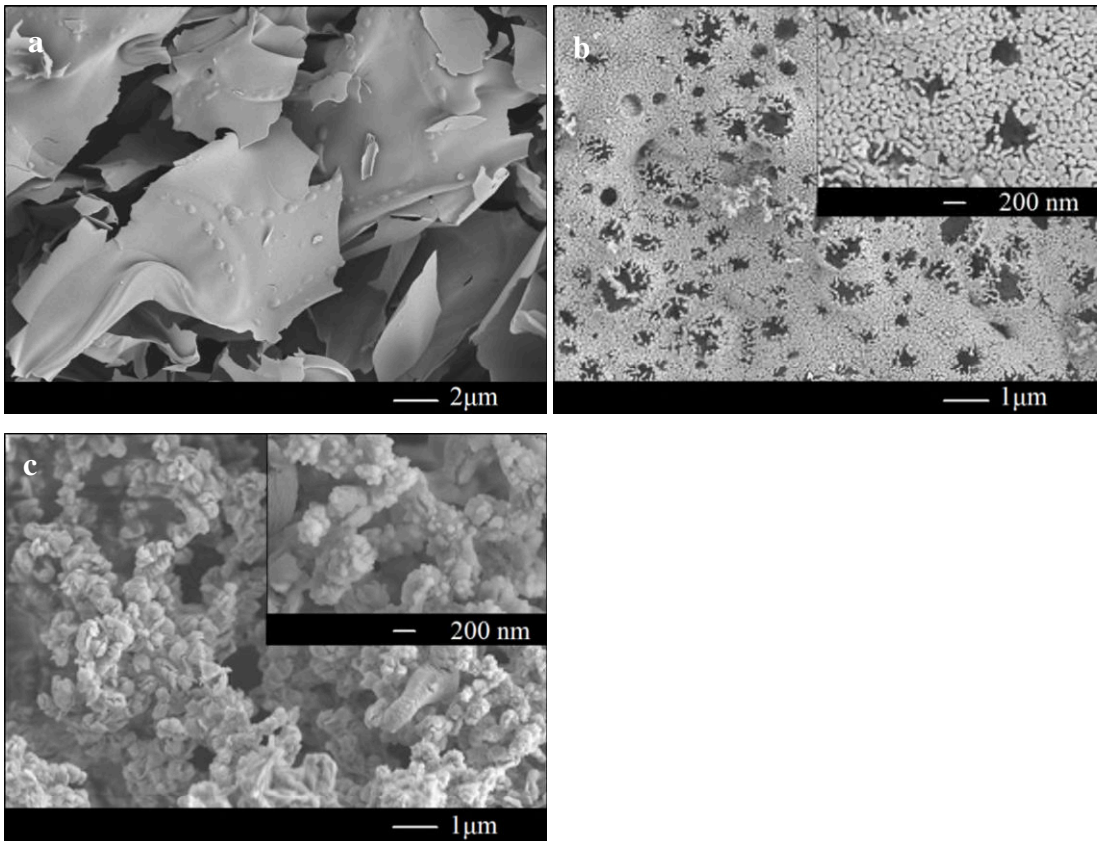

Fig. 4

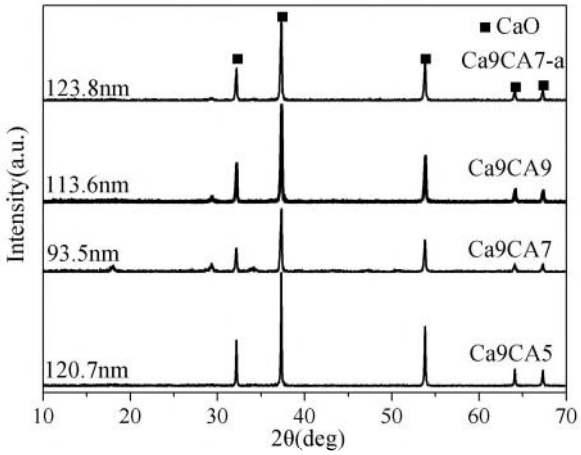
■ CaO
Ca9CA7-a
123.8nm
Ca9CA9
113.6nm
Ca9CA7
93.5nm
Ca9CA5
120.7nm
Intensity(a.u.)
10
20
30
40
50
60
70
2θ(deg)

Fig. 5

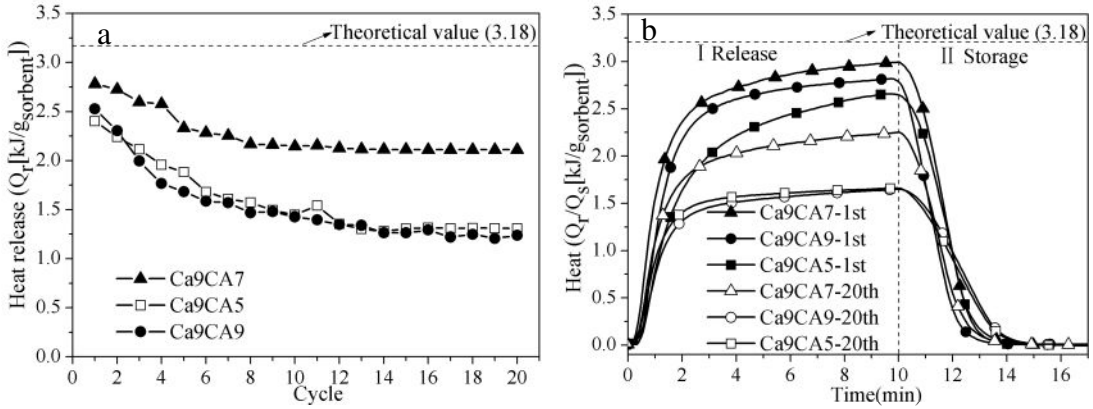
a
Theoretical value (3.18)
Heat release (Q_T[kJ/$g_{sorbent}$])
Cycle
Ca9CA7
Ca9CA5
Ca9CA9
b
Theoretical value (3.18)
I Release
II Storage
Heat (Q_T/Q_S[kJ/$g_{sorbent}$])
Time(min)
Ca9CA7-1st
Ca9CA9-1st
Ca9CA5-1st
Ca9CA7-20th
Ca9CA9-20th
Ca9CA5-20th

Fig. 6

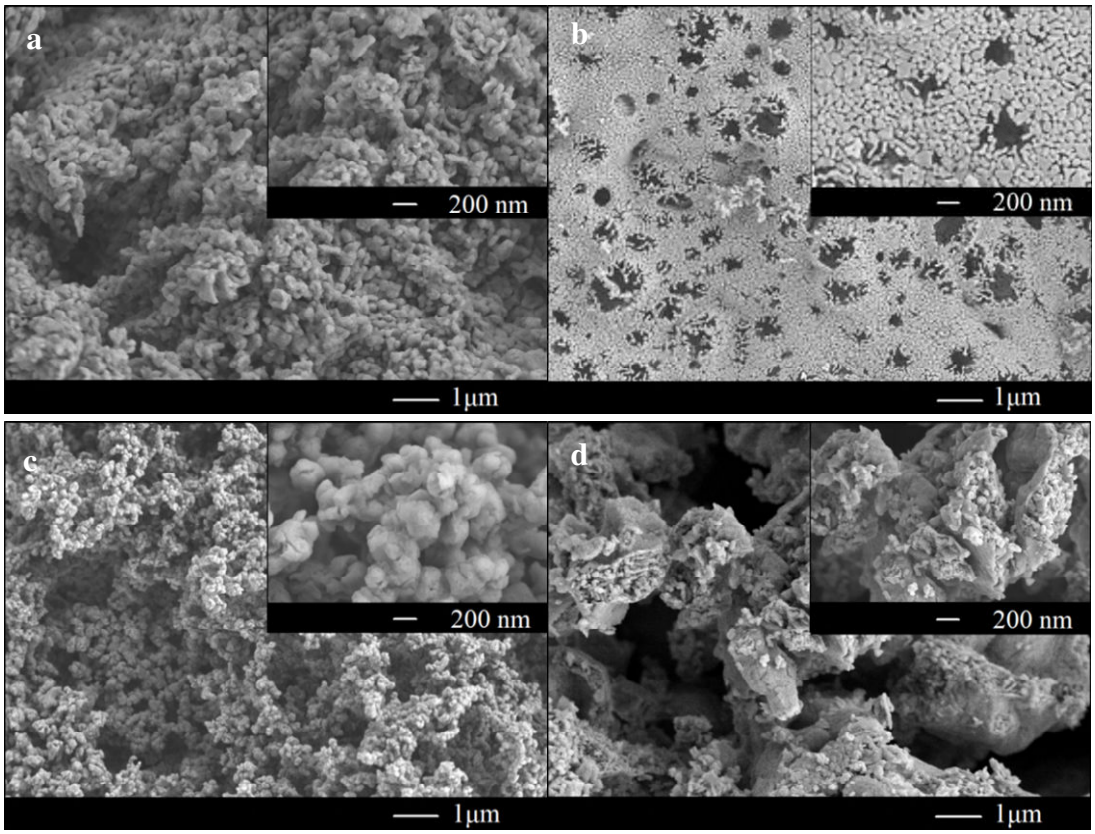

Fig. 7

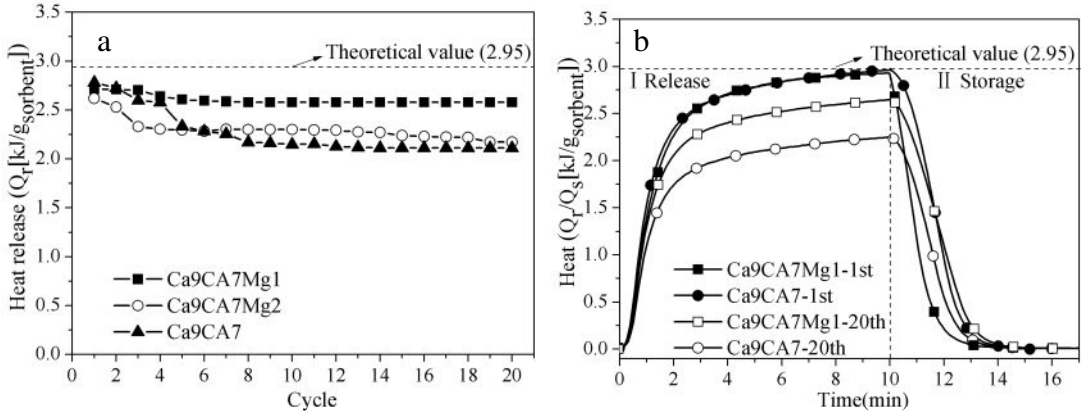
a
Theoretical value (2.95)
Heat release (Q_r[kJ/$g_{sorbent}$])
Cycle
Ca9CA7Mg1
Ca9CA7Mg2
Ca9CA7
b
Theoretical value (2.95)
I Release
II Storage
Heat (Q_r/Q_s[kJ/$g_{sorbent}$])
Time(min)
Ca9CA7Mg1-1st
Ca9CA7-1st
Ca9CA7Mg1-20th
Ca9CA7-20th

Fig. 8

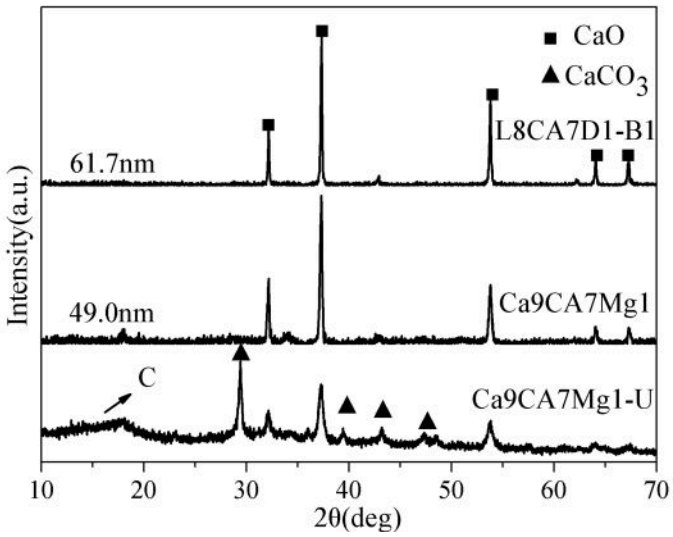
CaO
CaCO3
L8CA7D1-B1
61.7nm
Intensity(a.u.)
49.0nm
Ca9CA7Mg1
C
Ca9CA7Mg1-U
10
20
30
40
50
60
70
2θ(deg)

Fig. 9

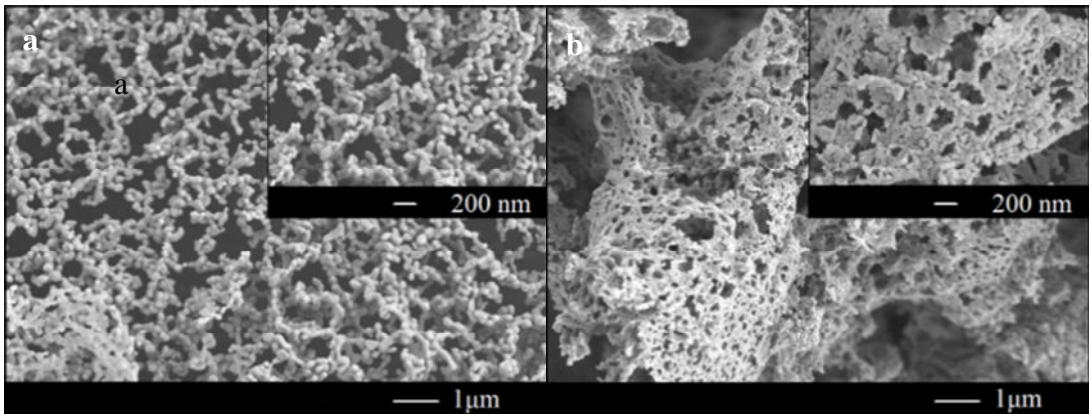

Fig. 10

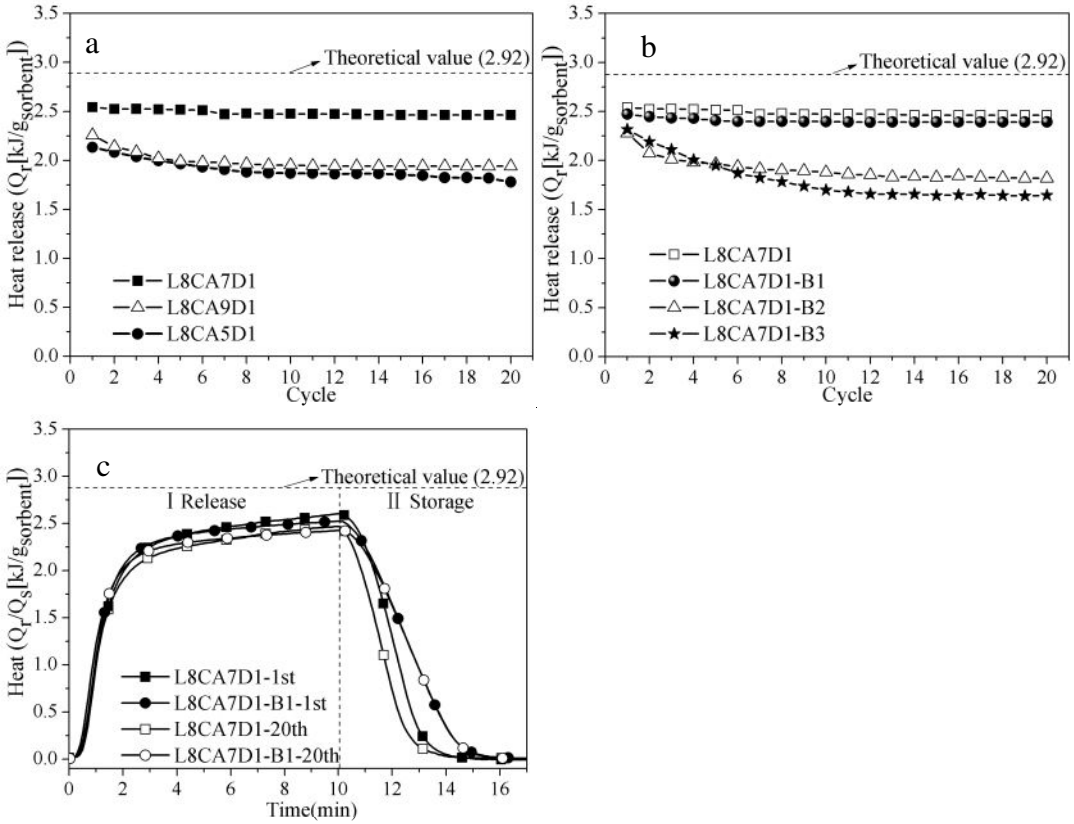
a
Theoretical value (2.92)
Heat release (Q_r[kJ/$g_{sorbent}$])
Cycle
L8CA7D1
L8CA9D1
L8CA5D1
b
Theoretical value (2.92)
Heat release (Q_r[kJ/$g_{sorbent}$])
Cycle
L8CA7D1
L8CA7D1-B1
L8CA7D1-B2
L8CA7D1-B3
c
Theoretical value (2.92)
I Release
II Storage
Heat (Q_r/Q_s[kJ/$g_{sorbent}$])
Time(min)
L8CA7D1-1st
L8CA7D1-B1-1st
L8CA7D1-20th
L8CA7D1-B1-20th

Fig. 11

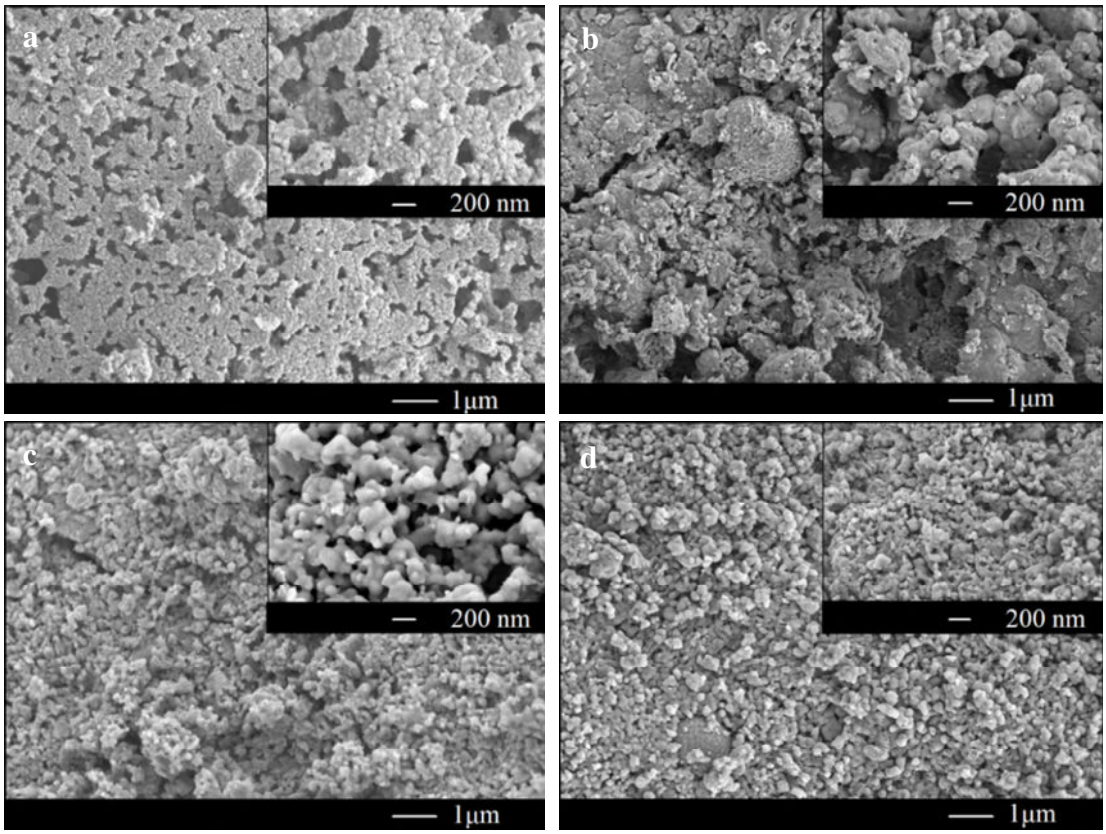

Fig. 12

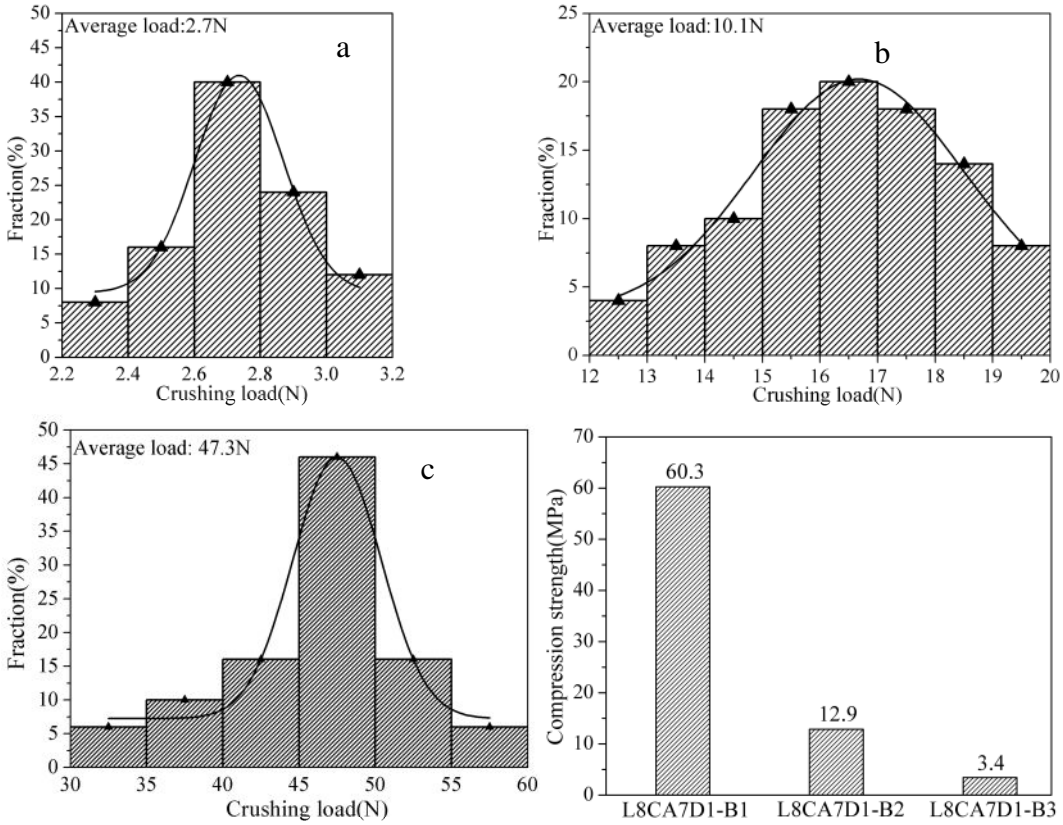
Average load:2.7N
a
Fraction(%)
Crushing load(N)
Average load:10.1N
b
Fraction(%)
Crushing load(N)
Average load: 47.3N
c
Fraction(%)
Crushing load(N)
Compression strength(MPa)
60.3
12.9
3.4
L8CA7D1-B1
L8CA7D1-B2
L8CA7D1-B3

Fig. 13